

A validated DEM modelling framework on plate and pile penetrations in a double-layer scour protection system

Shi, Hao; Cengiz, Cihan; Macaro, Giulia; Martinelli, Mario; Jovanova, Jovana; Schott, Dingena

DOI

10.1016/j.oceaneng.2024.120222

Publication date

Document Version Final published version Published in Ocean Engineering

Citation (APA)

Shi, H., Čengíz, C., Macaro, G., Martinelli, M., Jovanova, J., & Schott, D. (2025). A validated DEM modelling framework on plate and pile penetrations in a double-layer scour protection system. Ocean Engineering, 319, Article 120222. https://doi.org/10.1016/j.oceaneng.2024.120222

Important note

To cite this publication, please use the final published version (if applicable). Please check the document version above.

Copyright

Other than for strictly personal use, it is not permitted to download, forward or distribute the text or part of it, without the consent of the author(s) and/or copyright holder(s), unless the work is under an open content license such as Creative Commons.

Please contact us and provide details if you believe this document breaches copyrights. We will remove access to the work immediately and investigate your claim.

ELSEVIER

Contents lists available at ScienceDirect

Ocean Engineering

journal homepage: www.elsevier.com/locate/oceaneng



Research paper

A validated DEM modelling framework on plate and pile penetrations in a double-layer scour protection system

Hao Shi ^{a,*} , Cihan Cengiz ^b, Giulia Macaro ^b, Mario Martinelli ^{b,c}, Jovana Jovanova ^a, Dingena Schott ^a

- a Department of Maritime and Transport Technology, Faculty of Mechanical Engineering, Delft University of Technology, 2628CD Delft, the Netherlands
- ^b Deltares, 2629HV Delft, the Netherlands
- ^c Deptartment of Civil and Environmental Engineering, Carleton University, Ottawa, ON, Canada

ARTICLE INFO

Keywords: Scour protection Pile penetration Discrete element method Multispheres Calibration and validation

ABSTRACT

Monopiles are the dominant foundation type for offshore wind turbines, accounting for approximately 80% of the installed capacity. Installing offshore monopile foundations on seabeds susceptible to scour erosion requires monopiles to penetrate several pre-installed scour protection rock layers before securing them into the seabed. The accurate prediction of the pile penetration resistance is crucial to ensure successful monopile installations. To complement, and potentially reduce the dependence on the costly and labour-intensive experimental smallscale penetration tests, a numerical model has been developed using the Discrete Element Method (DEM) that captures the discrete nature of interactions between rocks and piles and predicts the resistance during the penetration process. The developed DEM model includes armour and filter rocks represented by multispheres and sand particles represented by spheres. A multistage calibration, verification and validation DEM modelling framework is proposed and examined with small-scale penetration tests conducted using plates and piles in a double-layer scour protection configuration. The sand material model is calibrated and verified using penetrometer tests and the rock material models are calibrated and verified using a plate penetration test. The DEM model with three verified materials predicts the penetration resistance well in small-scale pile penetration tests and proves the validity of the proposed framework. The DEM model presented in this paper facilitates the modelling in areas where traditional continuum-based numerical methods give less accurate predictions and provide insights that are difficult or nearly impossible to obtain through experimental methods.

1. Introduction

The construction of marine and offshore structures requires careful consideration of scour protection to ensure the stability and longevity of the installations. Scour protection is a critical component of infrastructure design in areas prone to erosion (Gerwick, 2007; Mayall et al., 2020; Mandviwalla and Christensen, 2021). Scour, the removal of sediment around structures due to flowing water, can compromise the stability and safety of various engineering works such as bridges, pipelines, and offshore platforms (Dahlberg, 1983; Cao et al., 2015). To mitigate the risks associated with scouring, engineers employ various techniques and materials to protect the foundations of these structures. One common method of scour protection is the use of riprap, which involves placing large rocks or concrete blocks around the base of a structure to dissipate the energy of flowing water and prevent erosion. Riprap is a

cost-effective and durable solution for protecting against scour, particularly in areas with high flow velocities or turbulent conditions (James and James, 2020; Singh et al., 2022). Another approach to scour protection is the use of geotextile mattresses, which are synthetic materials designed to reinforce soil and prevent erosion (Wang et al., 2023; Zhang et al., 2023a). Geotextiles can be combined with other scour protection measures, such as riprap or concrete mattresses, to provide additional stability and protection against scour. In addition to these traditional methods, new techniques are being developed to enhance scour protection. For example, scour monitoring systems can provide real-time data on erosion around structures, allowing engineers to assess the effectiveness of existing protection measures and make adjustments as needed (Winkler et al., 2023). Furthermore, advances in computational mechanics have led to the development of advanced and accurate numerical models, which are used to assess the impact of scour protection

E-mail address: h.shi-3@tudelft.nl (H. Shi).

^{*} Corresponding author.

during offshore wind turbine installations and operations (Zhang and Wang, 2015; Zhang et al., 2015, 2023b; Ma and Chen, 2021).

Among all types of offshore wind turbine foundations, monopiles remain the most common choice for offshore wind foundations, especially where water depths are less than 60 m. One key aspect of scour protection design is the assessment of monopile penetration into the seabed, as illustrated in Fig. 1, where a double-layer scour protection is deployed. Deeper penetration can provide greater stability and resistance to scour, while a shallower penetration may result in inadequate protection against erosion (Mayall et al., 2020; Whitehouse et al., 2011). Several factors influence the penetration depth of monopiles in scour protection design. These include the type of soil at the seabed, the size and shape of the monopile, the design of the scour protection system, and the environmental conditions at the site (OuYang et al., 2022). It is important to consider these factors to ensure that the monopile penetrates the seabed to an appropriate depth with effective scour protection that maintains its designed loading capacity.

With the rapid power growth of a single wind turbine generator, the outer diameter of the monopile foundation is expected to increase from around 8 m to above 12 m, leading to an increase in the rock size used for scour protection, especially on the large size armour rocks which are already above 200 mm (Whitehouse et al., 2011; DNV, 2022; Netherlands Enterprise Agency, 2022; Barbuntoiu and Thijssen, 2024). It is thus more challenging to estimate the resistance during the penetration process through the scour protection rock layer(s) and mitigate the installation risks. The most straightforward approach is to conduct field tests and formulate a validated mathematical model (Leimeister and Dose, 2018). However, this is very time-consuming, expensive and unpractical in most cases. An alternative and more cost-effective approach is to perform down-scaled experiments and obtain the relevant model at this scale, then use identified scaling laws to predict the behaviours at a large/field scale. A typical example is the physical modelling using a centrifuge test, where the load (gravity) acting on the soil specimen is artificially increased by the centrifugal force to represent the actual high load on the soil in the real field (Wang et al., 2021; Nietiedt et al., 2023a, 2023b).

Apart from experimental testing, numerical modelling techniques, such as finite element analysis (FEA), computational fluid dynamics (CFD) and discrete element method (DEM), are commonly used to assess the installations and operations of monopile foundations due to their flexibility and cost-effectiveness. For the loading and failure analysis of the installed monopile, FEA has proven to be the most suitable method. It assumes soil as a continuum body and deploys constitutive relations to properly simulate its mechanical behaviour and interactions with the monopiles, such as nonlinear hysteresis responses of monopiles during cyclic loading and the evolution of bending moment and lateral

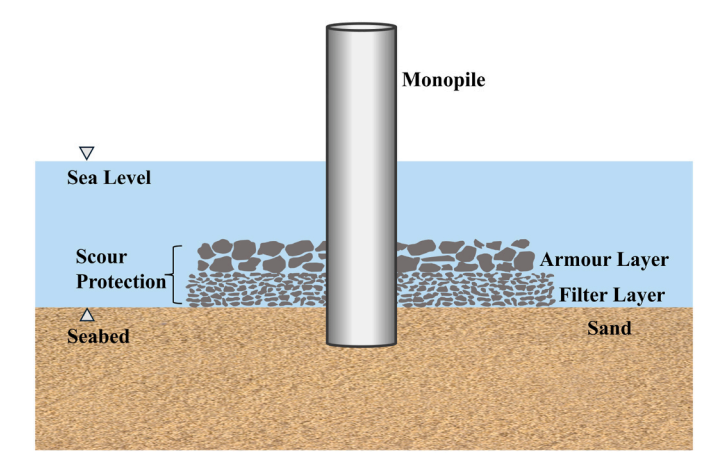


Fig. 1. Schematic illustration of monopile penetration in a double-layer scour protection arrangement.

responses (Cheng et al., 2021; Liu and Kaynia, 2022; Sarımurat, 2023). CFD, on the other hand, is widely deployed in studying hydrodynamics in offshore engineering, e.g., flows around the monopile foundations (Chen Ong et al., 2017; Zhai and Christensen, 2022) and fluid-structure interactions (Jaiman et al., 2010; Tran and Kim, 2018; Varelis et al., 2021; Li et al., 2024). For the interactions between soil and structures during installation, DEM has gained popularity in the past decades as this method simulates the movements based on Newton's second law and interactions of each particle based on different contact laws and thus captures the discrete nature of the materials.

In the premise of modelling geometry penetration into soils, for example, Liu and Wang simulated the pile driving into the sand using a two-dimensional DEM model and investigated the effects of sample porosity, initial stress state and ratio of pile diameter to median particle diameter on pile penetration behaviour (Liu and Wang, 2016). Similarly, Esposito et al. studied the pile installation using 2D circular particles DEM and carried out a multi-scale sensitivity analysis on particle rotations and penetration velocity (Esposito et al., 2018). For three-dimensional DEM, Miyai et al. investigated the plate penetration into glass beads with different plate thicknesses to particle median diameter ratio using quasi-two-dimensional DEM simulations and identified the ratio that changes the resistance fluctuations qualitatively (Miyai et al., 2019). Using 3D DEM with spherical particles, Cerfontaine et al. studied the silent piling of a cluster of four piles that progressively pushed into a sand bed by successive jacking sequences (Cerfontaine et al., 2021a). They also further investigated the influence of particle upscaling technique or pile penetration rate on the accuracy of simulating a screw pile installation process (Cerfontaine et al., 2021b). Gezgin et al. utilised both sphere and two-spheres to investigate the influence of particle aspect ratio and soil characteristics on the pile penetration process (Gezgin et al., 2022). In addition, with the upscaled spherical particles, Cerfontaine et al. investigated the potential plugging effect during an open-ended pile installation in a calibration chamber with both plain and rotary jacking (Cerfontaine et al., 2023). However, most of these models focused only on a single (sand) material using simplified spheres and were not validated against experimental tests.

Therefore, in this work, we aim to develop a multi-material DEM model of penetration tests and validate it against small-scale experiments. A multi-material DEM calibration, verification and validation framework will be examined by plate and open-ended pile penetration tests in a double-layer scour protection setting. Three main challenges will be addressed during the examination of this framework: i) modelling non-spherical particle shapes, e.g., scour protection rocks, ii) modelling more than a single material, e.g., sand; iii) determination of DEM material model parameters via calibration, verification and validation. This paper is structured as follows. In Section 2, we provide an in-depth explanation of the method employed, i.e. the Discrete Element Method (DEM), detailing the simulated materials, the contact model parameters and the setups used. Section 3 presents the concept of model calibration, verification and validation framework and the calibration of sand material. Section 4 further explains the application of the full framework to two different types of rocks used in this study. The method to identify the dominant DEM parameters using the numerical Design of Experiment (DoE), and calibration and validation using two separate laboratory penetration experiments are also addressed. Finally, in Section 5 we conclude with our main findings and further work.

2. Materials and methods

2.1. Discrete element method

For spherical particles and multispheres, our DEM model employs the Hertz-Mindlin (no-slip) (Mindlin, 1949, 1964; Di Renzo and Di Maio, 2005; Zhu et al., 2007) contact model with elastic-plastic (Type C) rolling friction (Ai et al., 2011; Wensrich and Katterfeld, 2012) that has been widely used for non-cohesive bulk materials, such as rocks &

pellets (Tripathi et al., 2021; Chakrabarty et al., 2022). Fig. 2 gives a schematic representation of the forces between two spherical particles' contact in DEM. The contact forces between two particles are calculated using a spring dashpot model in both normal and tangential directions. In the Hertz-Mindlin contact model, the normal and tangential springs are non-linear following the Hertzian and Mindlin theories. For modelling the rotational resistance and energy loss during rotation, the elastic-plastic (Type C) rolling friction model is chosen as it includes non-viscous damping torque and offers greater stability than other rolling models, such as standard or relative velocity dependent (RVD) rolling friction models. For detailed equations and further information on the contact model, readers are referred to the relevant literature (Zhu et al., 2007; Ai et al., 2011; Wensrich and Katterfeld, 2012; Tripathi et al., 2021; Chakrabarty et al., 2022).

In the current work, Altair EDEM (version 2022.3) and Altair HyperStudy (version 2022.3) software packages are employed. This is a suitable solution to simulate both spherical and non-spherical (multispheres) particles, where the latter requires the utilisation of graphics processing unit (GPU) computing for the sake of computational efficiency. The simulations are all conducted on a dedicated workstation with NVIDIA RTX A6000 (48 GB) GPU card.

2.2. Materials and their intrinsic parameters

A double-layer scour protection system contains 3 different materials: armour rocks ($d_{50} = 25$ mm), filter rocks ($d_{50} = 6.5$ mm) and sand ($d_{50} = 0.28$ mm), as shown in Fig. 3. These materials are used in the realworld penetration experiments performed in the Water and Soil Flume facility located at Deltares in Delft, the Netherlands. As we deploy the Hertz-Mindlin contact model with elastic-plastic (Type C) rolling friction, there are more than 10 model input parameters for each material, resulting in over 30 different parameters. To give a clear overview of these parameters, we categorise them into three types: intrinsic material properties; morphological parameters and interaction parameters. The intrinsic material properties include particle (solid) density, shear/bulk modulus and Poisson's ratio and the values deployed here are summarised in Table 1. The intrinsic material properties stay unchanged in the whole study. It is a common practice in DEM modelling to use softer particles when the shear modulus does not significantly influence the

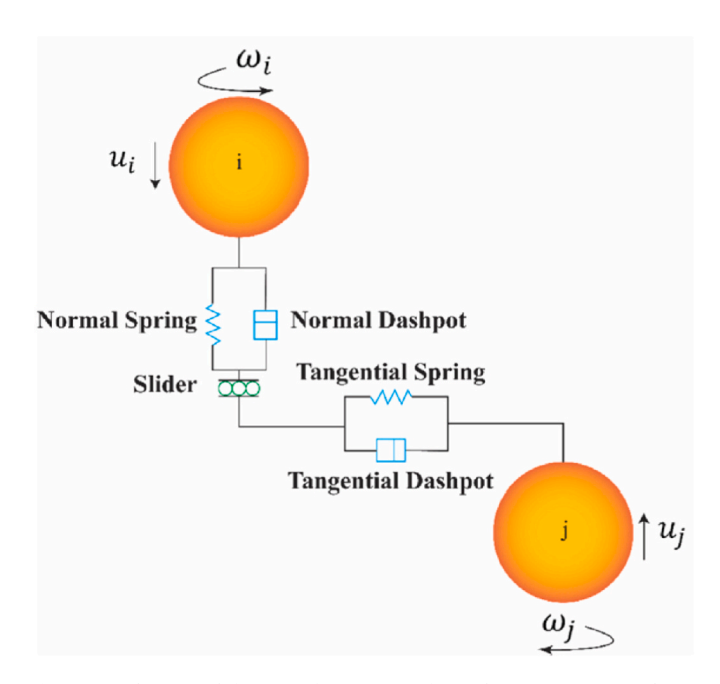


Fig. 2. A schematic definition of interaction forces between two particles in DEM (Hadi et al., 2024).

material bulk behaviour (Lommen, 2016; Lommen et al., 2019; Mohajeri et al., 2020). As we study large deformations originating from particles' rearrangements, we also deploy a shear modulus that is lower than the actual rock modulus.

The morphological parameters only apply to particles and include both particle size distribution (PSD) and particle shapes. Fig. 4 illustrates the particle size distributions of all three materials measured by the sieving method. As the armour rock size is about 100x larger than the sand particle, we scaled the sand particles by a coarse grain factor of 10 to reduce the number of sand particles to the order of magnitude in millions and achieve a feasible computational time that falls within a few days. Even after the coarse-graining of sand particles, the size ratio between armour rock and sand is still around 10. However, it is not possible to further increase the size of sand particles as the size distinction needs to be captured between the filter rocks and coarse-grained sand particles.

For particle shape, spheres are well-suited for sand particles since the original sand particles are nearly round and spherical and a single coarse-grained sand particle represents multiple original (unscaled) sand particles. However, the rock particles are mostly non-spherical (Fig. 3), and using spherical particles with rolling friction cannot capture the actual mechanical behaviour of the rock particles (Gezgin et al., 2022). Although the crushing and breakage of large particles may facilitate the particle arrangement, there was no breakage or crushing of rocks observed in the penetration experiments. Therefore, we assume no significant breakage/crushing at the small scale and adopt a clumped sphere approach to represent the irregular shape of both armour and filter rocks, as shown in Fig. 5. From each rock material, two rocks are selected and their surfaces are scanned to obtain the model rocks. The rocks are scanned using Qlone software and their scanned 3D surface model is further post-processed using Meshlab to reduce the number of mesh faces, typically from around 50000 faces to around 1000 faces. This is necessary to reduce the size of the shape model but pertaining the shape with a certain accuracy. The simplified shapes are then used to generate different multispheres that represent the original rock shapes. During the generation process, the Grid Constant (GC) and the smoothness factor (S) are chosen as 20 & 3 for armour rocks and 15 & 5 for filter rocks based on the computational efficiency. This results in 44 & 70 spheres for the two armour shapes (Figs. 5a), and 12 & 29 spheres for the two filter shapes (Fig. 5b), respectively.

2.3. Interaction parameters

Apart from the intrinsic material parameters, there are also interaction parameters which determine the key contact behaviours between particle-particle and particle-geometry, e.g., sliding friction, rolling friction and restitution coefficient. Within the scope of offshore scour protection, the rock layers are typically laid on top of the sand layer (seabed) and different types of rocks and sand are distinctively separated from each other. Therefore, we assume the interactions between the same material, i.e. sand-sand or rock-rock, are dominant over the interactions across different materials, i.e. sand-rock. The cross-material interaction parameters are then set to the same values as the interactions between the same material, i.e., sand-sand. An overview of defined interaction parameters related to sand is given in Table 2, where the cross-material interaction parameters (between sand and rocks) are kept the same as the interaction parameters between sand and sand. These defined interaction parameters are kept constant throughout the whole study while other cross-material interaction parameters between the filter and armour rocks can follow the analogy here and their determinations will be elaborated in detail in the calibration process.

2.4. Simulation setups

For calibration, sensitivity study, verification & validation purposes, three different simulation setups are employed in this work as shown in



Fig. 3. Materials used in this study (left to right): armour rocks, filter rocks and sand.

 Table 1

 Intrinsic material properties for all the materials used in this study.

| DEM Parameter | Unit | Sand | Filter Rock | Armour Rock | Geometry |
|---|------------------|--|------------------------|------------------------|------------|
| Density (ρ_s) Shear modulus (G) | [kg/m³] [GPa] | 2664 0.1 (Combarros Garcia et al., 2016) | 2680 0.1 | 2680 0.1 | 7850 78 |
| Poisson's ratio (v) | [-] | 0.25 (Combarros Garcia et al., 2016) | 0.3 (Bărbunţoiu, 2021) | 0.3 (Bărbunţoiu, 2021) | 0.28 |

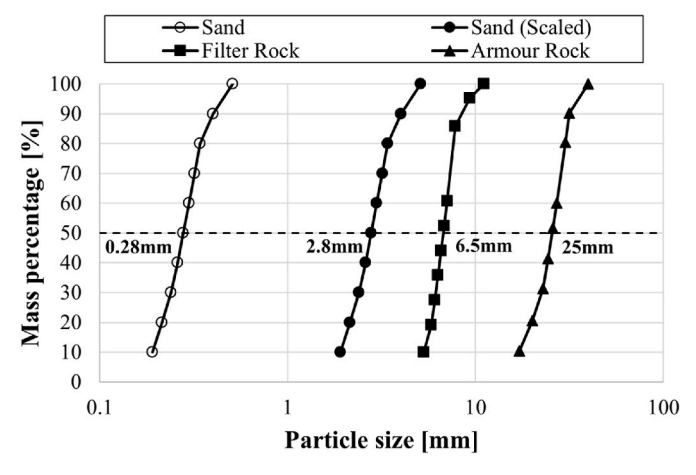


Fig. 4. Particle size distribution (PSD) for sand, filter and armour rocks.

Fig. 6, including the penetrometer test, the plate penetration box and the plate/pile penetration in double-layer scour protection. The penetrometer test (Fig. 6a) is typically used to test the uniformity of the soil and is a simplified version of the cone penetration test (CPT). The penetration cone has an 11.28 mm nominal diameter and 1 cm² cone tip area while the diameter of the penetration rod is 6 mm. The penetration velocity is kept constant at 30 mm/s with a penetration depth of 200 mm. The sand material is generated randomly in a rectangular domain with different volume fractions ($\varphi=0.55$ –0.66) using the volume packing method. The total number of spherical particles generated is approximately 320000 and 400000 for low and high-volume fractions, respectively. This setup is used for calibrating the packing density/volume fraction of the sandy soil underlying the rocks.

Fig. 6b illustrates the plate penetration box used for the sensitivity study on the DEM interaction parameters during plate penetration inside rock packing. This cubic box has a length of 750 mm with a steel bottom boundary (z-direction) and periodic boundaries in both the x & y directions. A steel plate with dimensions 500 mm \times 500 mm x 10 mm is driven into the rock packing at a constant velocity of 50 mm/s until 300 mm depth. Similar to the sand packing generation, approximately 17000 armour rocks (Fig. 5a) are randomly generated at the volume fraction φ

=0.5 and then settled to form the initial packing. By varying the frictional parameters between the rock particles, packings with different initial volume fractions can be obtained.

The last setup is the plate/pile penetration in double-layer scour protection, as shown in Fig. 6c. The material domain has an equal length (x-direction) and width (y-direction) of 850 mm and three different material layers along the height (z-direction): bottom sand layer (55 mm), middle filter layer (80 mm) and top armour layer (100 mm). Two geometries are deployed here: a steel plate with the dimensions 700 mm \times 500 mm x 10 mm and an open-ended steel pile with 323.9 outer diameter and 500 mm height. Unlike the plate, two different pile wall thicknesses are chosen here: 3 mm and 12.5 mm. The penetration velocity is kept constant at 50 mm/s and the depth stops at 200 mm where the geometry is getting into the bottom sand layer with the size of approximately one armour rock particle.

3. Modelling framework

3.1. Calibration, verification and validation

One of the most crucial aspects of DEM modelling is the calibration of the unknown model parameters, i.e. determination of the particleparticle and particle-geometry interaction parameters (Grima and Wypych, 2011). Two approaches are typically used to obtain these parameters: direct measurement and calibration using bulk experiments (Coetzee, 2017). For particles with idealised shapes and more uniform properties, such as glass beads, it is relatively easy to directly measure those interaction parameters at the particle scale with small-scale mechanical tests (Fuchs et al., 2014). For real-world granular materials, such as the rocks and natural sand used here, it is very cumbersome to measure those interaction parameters at the particle contact level and the measured parameters might not be representative of other particles in the same bulk due to the high variability of their shapes and surface roughness. Therefore, bulk experiments are often used for various applications with different flow regimes, e.g., angle of repose (Marigo and Stitt, 2015; Roessler and Katterfeld, 2018), drawdown test (Do et al., 2018), ring shear test (Mohajeri et al., 2020) and rotating drum (Coetzee, 2019).

The first DEM verification and validation (V&V) framework was proposed by Ooi (2013), where the verification process was defined as verifying that the DEM model implementation accurately reproduces the

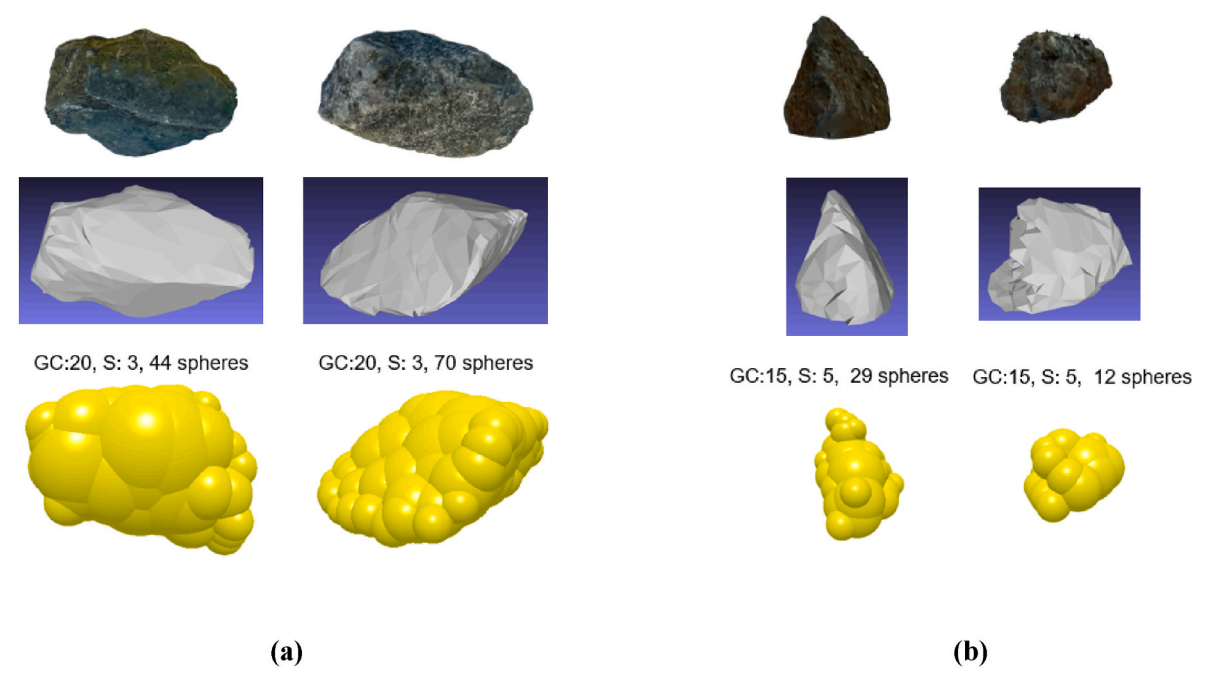


Fig. 5. Generation of non-spherical rock particles using surface scanning technique and multisphere approach: (a) two armour rocks, (b) two filter rocks. Top to bottom: original rocks, scanned shapes and corresponding multisphere representations.

Table 2An overview of the defined interaction parameters related to sand material.

| Interactions | DEM Parameter | Value |
|---------------------|----------------------------------|--------------------------------------|
| Sand-Sand | Sliding friction $(\mu_{s,p-p})$ | 0.64 (Combarros Garcia et al., 2016) |
| | Rolling friction $(\mu_{r,p-p})$ | 0.1 (Combarros Garcia et al., 2016) |
| | Restitution Coefficient | 0.75 (Combarros Garcia |
| | (e_{p-p}) | et al., 2016) |
| Sand-Geometry | Sliding friction $(\mu_{s,p-g})$ | 0.5 (Ucgul et al., 2015) |
| | Rolling friction $(\mu_{r,p-g})$ | 0.05 (Ucgul et al., 2015) |
| | Restitution Coefficient | 0.6 (Ucgul et al., 2015) |
| | (e_{p-g}) | |
| Sand-Filter & Sand- | Sliding friction $(\mu_{s,p-p})$ | 0.64 |
| Armour | Rolling friction $(\mu_{r,p-p})$ | 0.1 |
| | Restitution Coefficient | 0.75 |
| | (e_{p-p}) | |

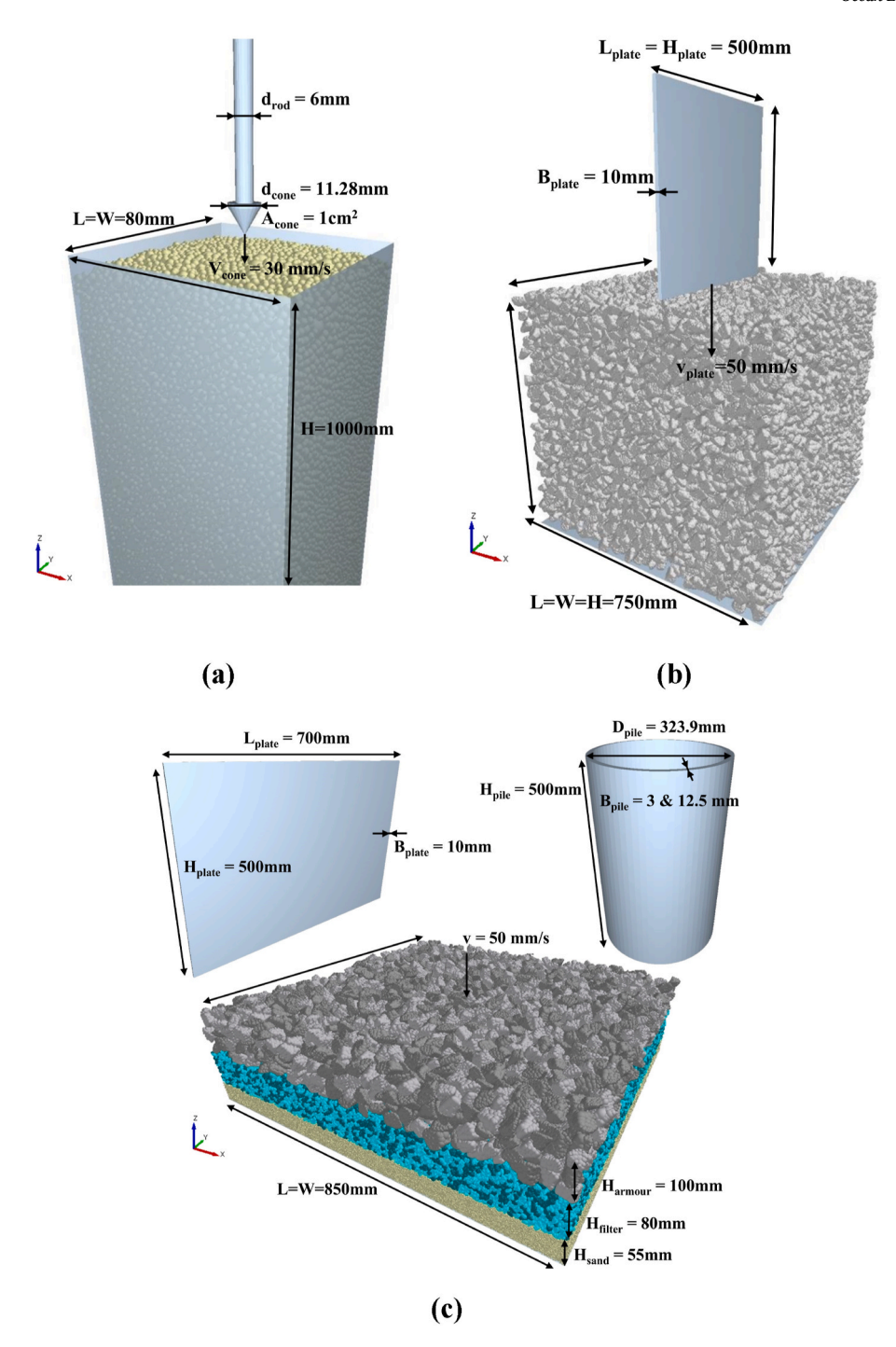
conceptual model and its solutions. In other words, it is the process of confirming the code implementation agrees well with benchmark (semi-)analytical solutions and evaluates the numerical errors from contact models/algorithms. This is a common step to test the reliability of a newly implemented DEM contact model and has to be performed before the calibration process. In the current study, verification refers to the process after the calibration of the contact model parameters. This is crucial in the determination of the right (most suitable) material interaction parameters as it is common to obtain multiple calibrated sets of parameters depending on the methods deployed. For validation, the verified (not just calibrated) set of parameters will be rerun in the DEM model and compared with the real-world experiment. Note that the experiments used for the calibration and verification processes cannot be used again in the validation process, and a different experiment needs to be employed such that the predictability of the verified model can be further tested.

The Calibration, Verification and Validation (CV&V) framework used in the current study is schematically illustrated in Fig. 7. In the calibration process, three experimental tests are used: penetrometer test, bulk density test and plate penetration test. Firstly, the sand model

parameters are calibrated using the penetrometer test and the corresponding simulation setup as given in Fig. 6a. Secondly, the penetration rock box setup (Fig. 6b) is used to generate initial packings and identify the sensitive model parameters and their validity ranges. Finally, the plate penetration in a double-layer scour protection (Fig. 6c) is simulated and the sensitive DEM model parameters (i.e. sliding friction coefficients) for filter and armour rocks are calibrated by performing the numerical Design of Experiments (i.e. full factorial) and then optimising towards the corresponding packing stiffness (slope of penetration resistance in armour or filter layer) measured in the real-world experiments. It is common to obtain multiple sets of calibrated parameters, depending on the number of model parameters and the optimisation algorithms deployed. Not all the calibrated parameter sets can represent the material behaviour we observed in the experiments and thus additional verification simulations were performed with these calibrated parameter sets and compared them against the experiments that were used for calibration, which in our case the plate penetration in a doublelayer scour protection. Once the agreement between the simulation and experiment is achieved, the sets of calibrated parameters are fixed and the DEM material models are verified. In the validation (prediction) process, the verified DEM material models stay unchanged while the geometry used in the penetration process is changed from a plate to a pile, as shown in Fig. 6c. Furthermore, two wall thicknesses (3 & 12.5 mm) are chosen here which differ from the wall thickness of the plate used earlier and the simulation outcomes are compared with corresponding experiments to evaluate the predictability of verified DEM material models.

4. Results and discussion

The results and discussions are presented here in four sub-sections. In Section 4.1, the calibration and verification of sand material are explained. In Section 4.2, we look at the plate penetration inside a rock box and identify the dominant interaction parameters. Section 4.3 is devoted to the calibration and verification of the identified dominant interaction parameters on plate penetration inside a double-layer scour protection. Finally, in Section 4.4, the verified DEM material models are further validated using piles with different wall thicknesses and the



 $\textbf{Fig. 6.} \ \ \textbf{The simulation setups employed in this work: a) penetrometer test, b) plate penetration box, and c) plate/pile penetration in double-layer scour protection.}$

model predictability is also discussed.

4.1. Calibration of sand material

For calibration of the sand material, the penetrometer test is used as shown in Fig. 6a. The original sand particles are too small in comparison with the rocks and simulating original sub-millimetre-sized particles in a meter-sized domain is not practical. Therefore, the coarse grain technique (Combarros Garcia et al., 2016) is used here to reduce the computational cost and the original sand particles are scaled up by a factor of 10 resulting in the particles that are slightly smaller than the size of the filter rocks (Fig. 4). For completeness and clarity, the full overview of both defined and calibrated DEM model parameters of

sand-sand and sand-geometry interactions are summarised in Table A1 in the appendix. The interaction parameters without references are directly measured from the North Sea sand used in this study. Note that the particle density (1664 kg/m³) used here is lower than the actual sand particle density (2664 kg/m³) due to the buoyancy force experienced in the fully submerged condition and the reduced particle densities are also applied to filter rocks, armour rocks and the geometries.

In the penetrometer test, one of the key parameters that determines the sand bed resistance is the bulk density/packing volume fraction. The typical values of volume fraction, φ , range from 0.55 to 0.66 for loose and dense packings, respectively. Different initial packings are randomly generated in this volume fraction range for the numerical penetrometer test and the results are compared with experimental

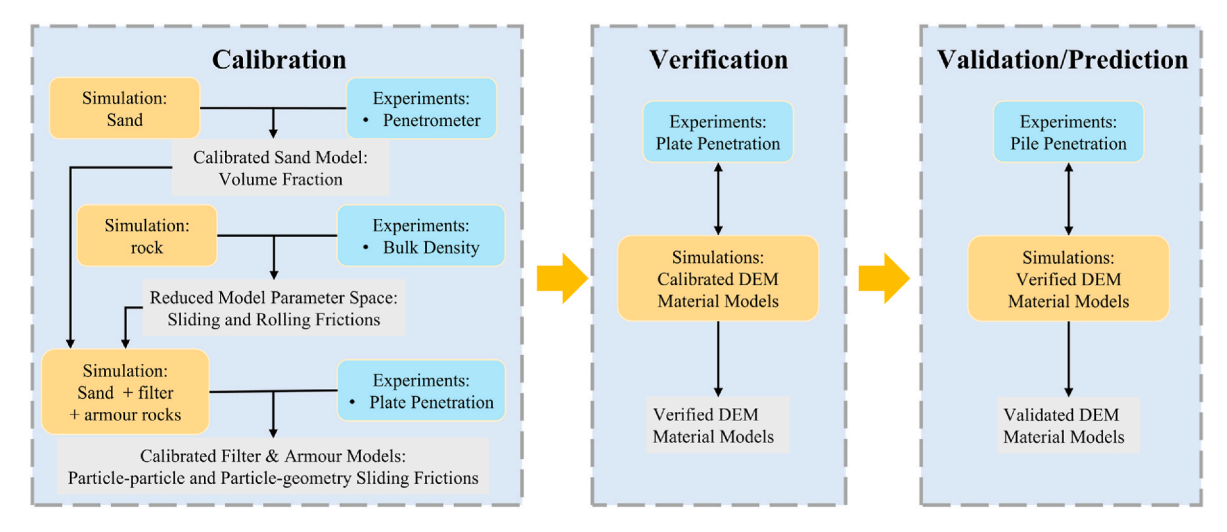


Fig. 7. The Calibration, Verification and Validation (CV&V) framework deployed for multi-materials DEM modelling.

penetrometer tests as shown in Fig. 8. Firstly, the stress measured on the cone tip during the penetration process is illustrated in Fig. 8a. The blue dashed line represents the mean of the 5 experimental measurements and the blue area indicates the range of deviations. The three dotted lines and three solid lines are the simulations with different initial packing volume fractions, ranging from 0.55 to 0.66. At the first 50 mm penetration depth, the simulation with the densest volume fraction of 0.66 agrees well with the experiment, all the other volume fractions show stresses lower than the experiments. When penetrating at a depth deeper than 50 mm, the simulations with volume fractions 0.62 (cyan dotted) and 0.63 (black solid) fall within the range of the experiments.

H. Shi et al.

Since the fluctuations of the stress field are high and both volume fractions 0.62 and 0.63 fall within the experimental deviations, it is difficult to conclude a single volume fraction value that has the best agreement with the experiments. Therefore, we include the work done during the penetration which is integral to the penetration force/resistance over the depth, as shown in Fig. 8b. It is clear that the simulation of the 0.62 vol fraction matches the lower bound of the experiments while the 0.63 vol fraction agrees well with the mean of the experiments. Therefore the 0.63 vol fraction in the simulation is selected as the calibrated value to represent the sand soil in the experiments. The bottom sand soil layer, cf. Fig. 6c, can then be generated with the calibrated initial volume fraction of 0.63. This single sand layer has dimensions of

 $850~\text{mm}\times850~\text{mm}$ x 55 mm and contains 2.53 million coarse grained sand particles that are feasible to be simulated with a small CPU cluster or a single GPU card.

4.2. Identification of dominant interaction parameters using rock box

4.2.1. Packing generation – experimental and numerical packing volume fraction

To obtain the initial packing volume fractions of the two rocks, bulk density tests are carried out with a customised container that has approximately 360 L internal volume as shown in Fig. 9. For each test, approximately 180L of rocks were filled into the container and the filled-in mass was measured with 5 repetitions of each rock type.

The experimentally measured bulk densities are $1457 \pm 26 \text{ kg/m}^3$ and $1608 \pm 9 \text{ kg/m}^3$ for filter and armour rocks, respectively. By dividing the bulk density by the skeleton density of rocks (2680 kg/m^3), the corresponding volume fractions 0.54 ± 0.01 and 0.60 ± 0.01 are obtained. From previous studies (Lommen et al., 2019; Huang et al., 2014; Shi et al., 2020), the interparticle frictions, cohesions and particle shapes are the dominating factors for the volume fractions. As the particle shapes are fixed from 3D surface scanning and no cohesions are involved in the coarse particles, the interparticle frictions (sliding $\mu_{s,p-p}$ and rolling $\mu_{r,p-p}$) are the ones of interest. Therefore, these two

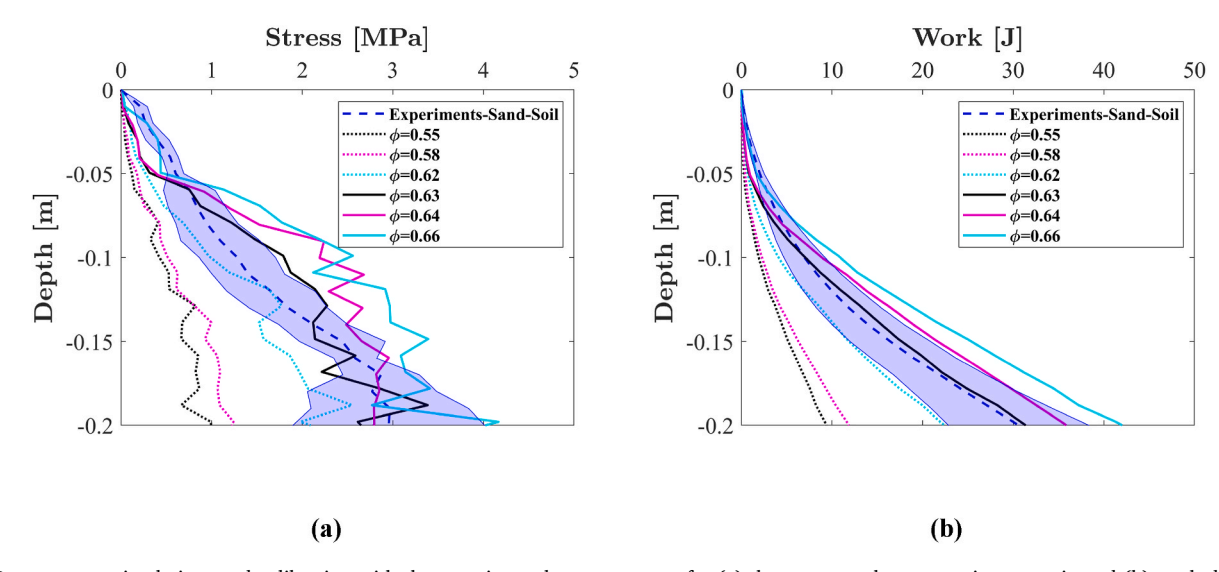


Fig. 8. Penetrometer simulations and calibration with the experimental measurements for (a) the stress on the penetration cone tip and (b) work done during penetration.



Fig. 9. Bulk density tests of filter rocks. The container has inner dimensions of 0.828 m \times 0.724 m x 0.6 m.

parameters are used to construct a DoE for the simulation of packing generation. Here, the setup in Fig. 6b is used without the plate geometry. 14934 multisphere particles (~0.88 million spheres) are randomly generated in this cuboid domain with an initial packing volume fraction of 0.49 and then settled for 1s process time. The timestep, $\Delta t = 4e$ -6s, is chosen as a 20% Rayleigh timestep that is calculated using the diameter of the smallest sphere inside the multisphere. The domain has a real wall at the bottom, a free surface at the top and side periodic boundaries. To identify the appropriate range of interparticle frictions that can achieve the low volume fractions measured in the experiments, a numerical Design of Experiments (DoE) is constructed with a full factorial design: $\mu_{s,p-p}$ and $\mu_{r,p-p}$ are varied between 0.1 and 1.0 with ten equally spaced levels, resulting in 100 packing generation and settling simulations. The range of parameters chosen here is based on the realistic frictions typically used in the DEM studies for real-world materials, thus frictionless or very high frictions are out of the scope.

The effect of the interparticle sliding friction coefficient on the packing volume fractions after settling is depicted in Fig. 10. The minimum value to reach a volume fraction of 0.54 is $\mu_{s,p\cdot p}=0.3$ and above which is permissible to reach the target experimental volume fractions of rocks. Similarly, the minimum rolling friction can also be determined as $\mu_{r,p\cdot p}=0.5$. For the general effect of sliding friction, the increase of $\mu_{s,p\cdot p}$ from 0.1 to 1.0 results in a prominent decrease of packing volume fraction from 0.620 to 0.495. Along the $\mu_{s,p\cdot p}=0.3$ line, the effect of rolling friction is also given by different colours. With increasing the rolling friction coefficient $\mu_{r,p\cdot p}$ from 0.1 (blue) to 1.0 (red), the packing volume fraction changes from 0.564 to 0.537, which is much less than

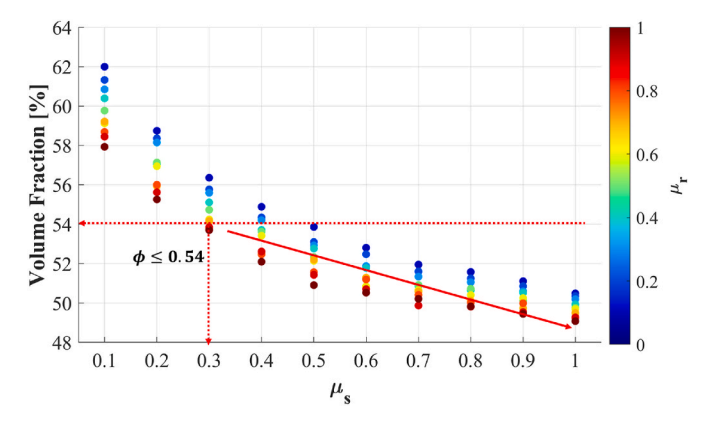


Fig. 10. Packing volume fractions after generation and settlement using the full factorial DoE: effect of interparticle sliding friction coefficient: $\mu_{s,p-p}$.

the effect of sliding friction. Normally the rolling friction has a more prominent effect on packing volume fraction than sliding friction, however, in the current case, the particle shapes are modelled by multispheres, thus the rolling friction that represents the shape of particles becomes less dominant.

4.2.2. Screening Design of Experiments - Plackett-Burman

After the determination of the ranges of both sliding and rolling friction coefficients, another numerical DoE is needed to identify the most influential material interaction parameter(s) during the penetration process. There are 7 free parameters utilised in the Hertz-Mindlin with elastic-plastic (Type C) rolling contact model and if we make a full factorial DoE on these 7 parameters and each parameter has two levels/values, it will require 128 simulations. A single penetration simulation with 200 mm depth and 10 mm/s penetration speed needs a 6–7 h runtime, resulting in about 1-month simulation runtime, which is unfavourable. To confront this challenge, we utilise a screen design method, namely the Plackett-Burman (P-B) design (Antony, 2023; Emmerink et al., 2023) to reduce the computational costs.

The Plackett-Burman design is an efficient statistical method used for screening a large number of factors to identify the most significant ones affecting a process or outcome. For a 7-parameters design, only 8 runs are required as shown in Table 3. The "+1" and "-1" refer to the high and low levels (values) of each parameter, which are given in the second row of the table. For interparticle sliding and rolling frictions, the low levels are taken from the packing generation results. Whereas other parameters' levels are determined by reviewing values used in previous relevant studies (Lommen, 2016; Bărbunţoiu, 2021; Imre et al., 2008; Durda et al., 2011; Sandeep et al., 2021; Hageman, 2022).

The effect of 7 contact model parameters on the penetration force is shown in Fig. 11. The first three parameters, namely particle-particle sliding friction coefficient $\mu_{s,p-p}$, particle-geometry sliding friction coefficient $\mu_{s,p-g}$ and particle-particle restitution coefficient e_{p-p} , contribute to 73% sensitivity of penetration force. Both $\mu_{s,p-p}$ and $\mu_{s,p-g}$ are dominating/sensitive parameters as each of these two parameters occupy 31% and 28% of the total contribution, respectively. The particle-particle restitution coefficient e_{p-p} sits in third place and has a 14% contribution, which is around half of the contribution of $\mu_{s,p-g}$. The rest of the parameters all have contributions of less than 10% and are categorized as insensitive parameters.

4.2.3. Effect of inter-particle restitution coefficient

As the parameter e_{p-p} has a contribution of 14%, the significance of this parameter is not clear. Therefore, extra plate penetration simulations are performed to gain further insights into this aspect, which allows us to determine the sensitivity thereof. The particle-particle restitution coefficient is varied between high and low levels as in the P-B design (0.05 and 0.95) and 5 different initial packings are randomly generated to reveal the variability caused by different initial packings.

In Fig. 12, the effect of the particle-particle restitution coefficient on the penetration work is given for 50 mm/s penetration velocity using the

Table 3Plackett-Burman screen design of 7 material interaction parameters.

| Run | G_p | $\mu_{r,p-p}$ | $\mu_{r,p-p}$ | $e_{p	ext{-}p}$ | $\mu_{s,p-g}$ | $\mu_{r,p-g}$ | $e_{p	ext{-}g}$ |
|-----|-------|---------------|---------------|-----------------|---------------|---------------|-----------------|
| | 5e7 | 0.4 | 0.5 | 0.05 | 0.1 | 0.1 | 0.05 |
| | 5e9 | 1.0 | 1.0 | 0.95 | 1.0 | 1.0 | 0.95 |
| 1 | +1 | +1 | +1 | -1 | +1 | -1 | -1 |
| 2 | -1 | +1 | +1 | +1 | -1 | +1 | -1 |
| 3 | -1 | -1 | +1 | +1 | +1 | -1 | +1 |
| 4 | +1 | -1 | -1 | +1 | +1 | +1 | -1 |
| 5 | -1 | +1 | -1 | -1 | +1 | +1 | +1 |
| 6 | +1 | -1 | +1 | -1 | -1 | +1 | +1 |
| 7 | +1 | +1 | -1 | +1 | -1 | -1 | +1 |
| 8 | -1 | -1 | -1 | -1 | -1 | -1 | -1 |

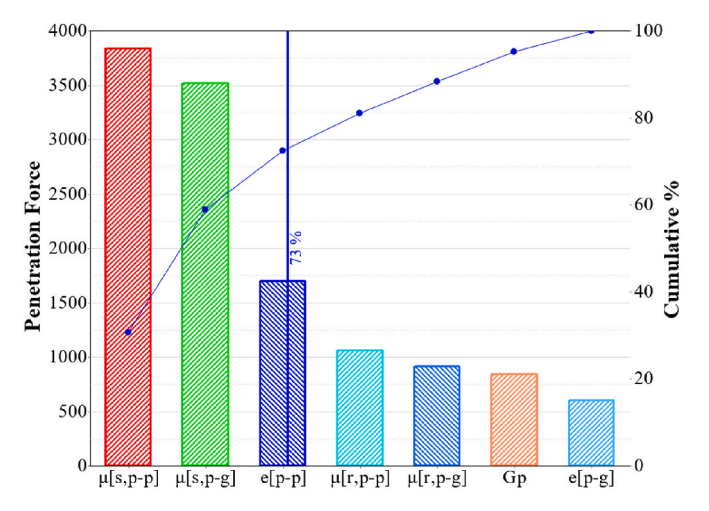


Fig. 11. Pareto plot: effect of 7 contact model parameters on the penetration force evaluated from P-B design.

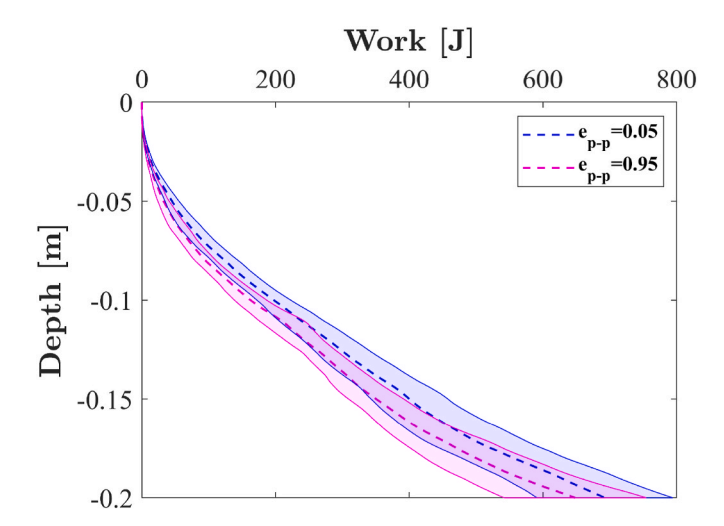


Fig. 12. Effect of particle-particle restitution coefficient $e_{p\cdot p}$ on the penetration work.

work done during penetration. The dashed lines are the means of the 5 simulations with different initial randomly generated packings and the coloured shading areas are their standard deviations. Within 0.2 m penetration depth, there is no significant effect of restitution coefficient observed on the penetration work, the difference due to varying the particle-particle restitution coefficient (0.05–0.95) falls within the ranges of the standard deviations. Therefore, the particle-particle restitution coefficient $e_{p\cdot p}$ is insignificant during the plate penetration and will be kept at 0.5 for all future simulations. Similarly, other insensitive parameters identified from the P-B design are all fixed for calibration and validation processes, which reduces the total number of free interaction parameters and leaves only $\mu_{s,p\cdot p}$ and $\mu_{s,p\cdot p}$ for further calibrations.

4.3. Plate penetration in double-layer scour protection

Now we have the sand material ready and rock materials where each has two free interaction parameters to be calibrated and verified. For calibration and verification, the setup of plate penetration in a double-layer scour protection (Fig. 6c) is used.

4.3.1. Determination of bottom domain boundary

To understand the boundary effect at the bottom of the material domain (underneath the 80 mm filter rock layer), six different

boundaries are generated: rigid bottom boundary without sand, 50 mm thick sand layer, 150 mm thick sand layer, 50 mm thick extra filter layer, 150 mm thick extra filter layer and 300 mm extra filter layer. The plate penetrates with 10 mm/s constant penetration velocity until 200 mm depth, except for the case of the 150 mm thick sand layer, where a 250 mm penetration depth is deployed.

The penetration resistances of the six different bottom boundaries are shown in Fig. 13. For the first 150 mm penetration depth, all six boundaries show very similar resistances, with rigid boundary conditions showing slightly lower resistance at the beginning of the penetration. When the penetration depth is larger than 150 mm, the rigid boundary and 50 mm extra filter layer give similar overshooting to unrealistic force values, while the penetration force measured by the 50 mm sand boundary agrees well with the force from the 150 mm sand boundary, with a slightly stiffer behaviour at the first 30 mm penetration depth. For the case of 150 mm and 300 mm extra filter layers, the penetration force increases monotonically with the depth, which gives a stiffer bottom boundary and is qualitatively different from that of the sand boundary layer. Therefore, a 50 mm sand layer is chosen to cover both the real soft bottom boundary as well as the computational efficiency.

4.3.2. Determination of penetration velocity

In penetration experiments, 11 mm/s velocity was used to minimise the dynamic effect during the penetration process. The simulations shown in the previous section are carried out at 10 mm/s penetration velocity with 20 s process time. For experiments, a lower penetration velocity is more favourable due to the data logging aspect, however, this limitation is not present in the numerical simulations. It is thus favourable to choose a higher velocity to reduce the total simulation time. For an object penetrating a granular medium, the penetration velocity should be lower than the critical velocity to achieve a quasistatic penetration. This critical velocity is calculated as $v_c = \sqrt{2gd_p}/10$, where g and v_p are gravitational acceleration and particle diameter, respectively (Gezgin et al., 2022; Feng et al., 2019). For the armour and filter rocks, the critical velocity is between 40 and 70 mm/s, thus two lower velocities, 30 and 50 mm/s, are chosen here for further comparison.

The influence of penetration velocity on the penetration process is given in Fig. 14. Increasing penetration velocity from 10 mm/s to 50 mm/s gives a 5% increase in the penetration work. The standard deviations of 4.7% and 3.6% are obtained for 10 and 50 mm/s penetration velocities, respectively. The difference caused by increasing the penetration velocity is comparable to the difference obtained by different

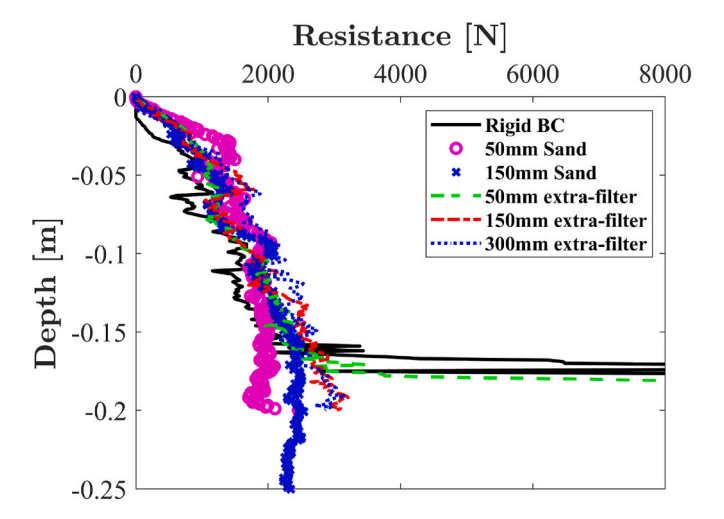


Fig. 13. Effect of the bottom boundary underneath the filter rocks on the penetration resistance.

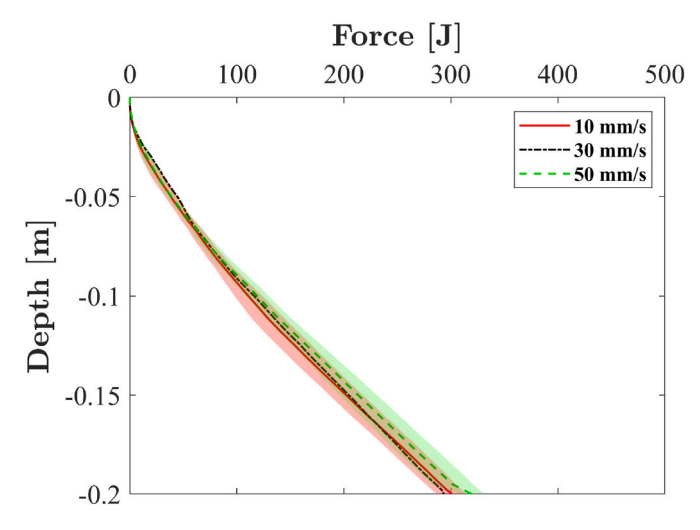


Fig. 14. Effect of the penetration velocity on the penetration resistance.

initial randomly generated packings, meaning the insignificance of the difference and thus the validity of using 50 mm/s penetration velocity. This results in a 5x speed up and an 80% reduction of the simulation time.

4.3.3. Calibration & verification of armour and filter layers

In total, 4 sliding friction coefficients need to be calibrated, 2 for armour rocks and 2 for filter rocks. Each sliding friction coefficient needs a minimum of 3 levels/values in a numerical DoE to form a full factorial design. There are in general two approaches to performing the calibration process: i) a full factorial DoE with 4 parameters and 3 levels of each parameter; ii) two full factorial DoEs with each DoE focus on a single material. Here, we choose the second approach as the frictional behaviour inside the filter layer has an insignificant influence on the frictional behaviour in the armour layer (when friction parameters are set to intermediate levels/values, data not shown here). This results in a full factorial numerical DoE of 9 simulations for a single material (Table 4, 18 simulations in total) and the total simulation time is reduced by a factor of 3, from ~30 days to ~10 days. The ranges of the two friction parameters are chosen based on the range used in the P-B design (Table 3). For the cross-material interaction parameters, such as armour-filter, filter-sand and armour-sand interactions, the values are all kept at the intermediate value used in the DoE, under the assumption that these types of interactions are secondary due to the layering design of the scour protections.

The calibration process is carried out in two steps: i) the frictional parameters of the armour layer were calibrated using the packing stiffness of the armour layer, i.e., the slope of 102 N/mm of the first 40 mm depth as shown in Fig. 15; ii) the frictional parameters of the filter layer were calibrated using the packing stiffness of the filter layer (20 N/mm)

Table 4The 3-level full factorial numerical calibration DoE for both armour and filter layers.

| Run | $\mu_{s,p-p}$ | $\mu_{s,p-g}$ |
|-----|---------------|---------------|
| | 0.4, 0.7, 1.0 | 0.4, 0.7, 1.0 |
| 1 | 0.4 | 0.4 |
| 2 | 0.4 | 0.7 |
| 3 | 0.4 | 1.0 |
| 4 | 0.7 | 0.4 |
| 5 | 0.7 | 0.7 |
| 6 | 0.7 | 1.0 |
| 7 | 1.0 | 0.4 |
| 8 | 1.0 | 0.7 |
| 9 | 1.0 | 1.0 |

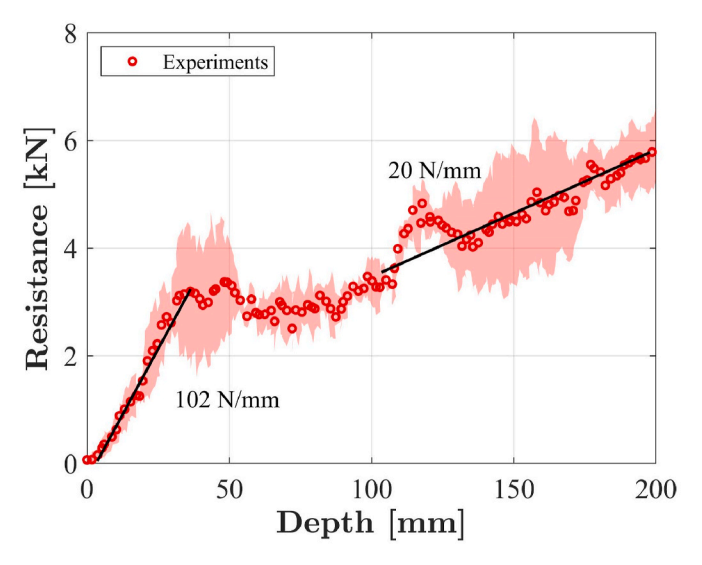


Fig. 15. Penetration experiments used for the calibration of the armour and filter layers. The slopes are obtained from linear regression fitting of 0–40 mm depth and 100–200 mm depth, respectively.

obtained within 100 mm and 200 mm depth. For each calibration step, the numerical DoE of 9 simulations were performed and results were then fed into the optimisation model to identify the parameter set that can reach the target armour rock packing stiffness. Here, two optimisation techniques were used: Genetic Algorithm (GA) (Mohajeri et al., 2020; Shapiro et al., 2001) and Global Response Search Method (GRSM) (Locatelli and Schoen, 2013; Horst and Pardalos, 2013; Pardalos and Romeijn, 2013). GA mimics natural selection, operating on string-encoded solutions through genetic operators like crossover and mutation, favouring the exploration of solution space. In contrast, GRSM is mathematically driven, refining solutions based on system responses to perturbations, prioritising exploitation. The genetic algorithm used here has also two variations in its surrogate models: linear regression (GA1) and Gaussian process regression (GA2). The optimisation objective is to find the frictional parameters that give the smallest error, which is the difference between the simulated packing stiffness and the experimentally measured stiffness. The system identification formulation is used here to minimise the sum of the normalised error squared,

 $\min\sum\left(\frac{f_i-T}{T}\right)^2$, where f_i is the *i*th response/stiffness from the iteration and T is the target packing stiffness. The calibrated parameter sets using different optimisation techniques are summarised in Table 5 for both armour rocks and filter rocks.

For armour rock, all three methods provide one optimal/calibrated parameter set. GA1 gives lower particle-geometry sliding friction while GA2 and GRSM give very similar calibrated parameter sets. For filter rock, the final calibrated frictions for both GA1 and GA2 are at the lower boundary of the DoE, while GRSM shows a distinct outcome compared to the other two methods. To verify the calibrated parameter sets obtained from different optimisation methods, the penetration simulations have been conducted using the three calibrated parameter sets and the penetration resistance and work done using the GRSM method show the

 $\begin{tabular}{ll} \textbf{Table 5} \\ \textbf{Calibrated particle-particle and particle-geometry sliding friction coefficients} \\ \textbf{using 3 different optimisation models}. \\ \end{tabular}$

| Method | Armour Rock | | Filter Rock | |
|--------------------|--|----------------------|----------------------|----------------------|
| | $\mu_{s,p-p}$ | $\mu_{s,p\text{-}g}$ | $\mu_{s,p\text{-}p}$ | $\mu_{s,p\text{-}g}$ |
| GA1 GA2 GRSM | 0.64 0.59 (Combarros Garcia et al., 2016) 0.58 | 0.42 0.91 0.95 | 0.40 0.40 0.72 | 0.40 0.40 0.88 |

closest response to the mean of the experiments, as depicted in Fig. 16. The model prediction matches very nicely with the experimental data for both the penetration resistance (Fig. 16a) and the work done (Fig. 16b). Now the DEM model for double-layer scour protection is fully calibrated and verified. For completeness and clarity, the full overview of both calibrated & verified DEM model parameters of armour and filter rocks interactions are summarised in Table A2 & A3 in the appendix.

4.4. Pile penetration in double-layer scour protection

The calibrated and verified DEM model developed for plate penetration needs to be further validated using pile penetration tests illustrated in Fig. 6c. The DEM model validation is to test the predictability or robustness of the calibrated and verified model using a different process or environmental/boundary conditions, which is covered by two aspects here: i) the shape of the penetration object is varied from a plate to a pile; ii) the wall thickness of the geometry is also varied using both thinner and thicker values, namely 3 mm and 12.5 mm.

4.4.1. Variations in initial penetration locations

In experiments, the variability is obtained by penetrating the pile at different locations. Similarly, in the validation simulations, for each pile wall thickness, triplet simulations are performed by shifting the initial pile locations for 50 mm in the x-direction to the origin, as shown in Fig. 17. As periodic boundary conditions are applied in both x- and y-directions, the outer pile edge distance is kept unchanged before and after shifting, which allows for capturing the variability due to the difference in the penetration path.

4.4.2. Validation of the verified model

The simulation results are validated against the experiments for both the 3 mm pile and 12.5 mm pile as shown in Fig. 18 using the penetration resistance. For the resistance of the 3 mm pile (Fig. 18a), the simulated penetration resistances agree well with the experiments within 50 mm and 150 mm penetration depth. For the first 50 mm penetration depth, a 4 kN peak resistance around 40 mm penetration depth is observed in the simulation while no peak is present in the experiment. However, for the three experimental tests carried out, only one experiment has a peak resistance at 30 mm penetration depth (individual data not shown in Fig. 18) and this peak resistance is averaged out when plotting only the mean of the three experimental tests. Furthermore, at penetration depth deeper than 150 mm, the simulated resistance is higher than the experiments, where the latter seems to reach a plateau.

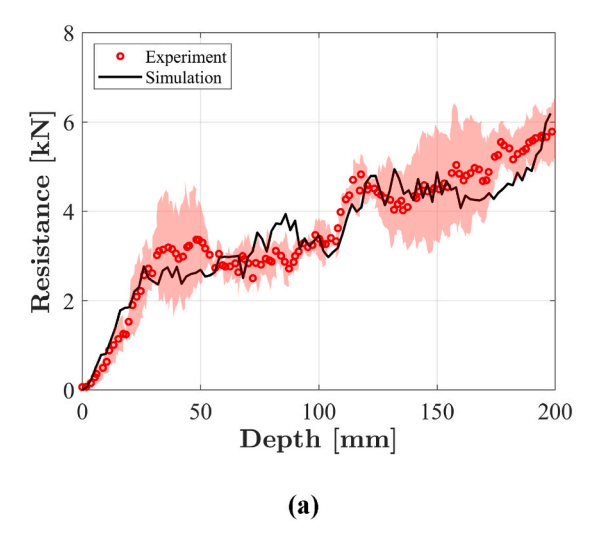
For the resistance of the 12.5 mm pile (Fig. 18b), the simulated

penetration resistance agrees nicely with the experiments within 180 mm penetration depth, which is the total thickness of both filter and armour layers. When penetrating deeper than 180 mm depth, the simulated penetration resistance deviates from the experiments as it gets closer to the bottom boundary at 250 mm depth which is around 2–3 armour rock size. In general, the calibrated and verified model predictions on the penetration resistance inside the scour protection (armour and filter) layers agree well with the experiments, which proves the validity of the calibrated and verified material model parameters as well as the calibration, verification & validation (CV&V) framework proposed here.

5. Conclusion

In this study, we proposed a novel DEM calibration, verification and validation framework to address the challenges that are commonly encountered for systems containing multiple granular materials. The proposed framework was successfully applied to the plate and pile penetrations in a double-layer scour protection system and resulted in good agreements with the experiments. The calibration procedure was conducted on each material and developed based on the sensitivity factors and computational constraints to reach a calibrated DEM model that includes sand, filter and armour rocks. The calibrated DEM model was verified using the plate penetration experiments and validated against the pile penetration experiments which have different wall thicknesses. Good agreements on the penetration resistance were achieved between the model predictions and the experimental measurements. The key conclusions and insights of this work are as follows.

- The sand material was calibrated using the cone penetrometer test
 and it is crucial to include a sand layer below the rock layers to form
 a soft and realistic boundary. Replacing the sand layer with a rigid
 wall or extra layer of rocks gives over-predictions of the penetration
 resistance when the penetration geometry is getting close to the
 bottom boundary.
- Bulk density (volume fraction), particle shape and interparticle
 frictions are key factors dominating the penetration resistance. When
 multispheres are used instead of spheres for modelling the rock
 shapes, the particle-particle rolling friction becomes less sensitive
 contributing to the penetration resistance.
- Using the screen and full factorial designs of numerical DoE can reduce the number of parameters and the space of the sensitive parameters. The number of calibration parameters is reduced from 7 to 2 by the screen design of the plate penetration box simulation while the lower bound of particle-particle and particle-geometry sliding



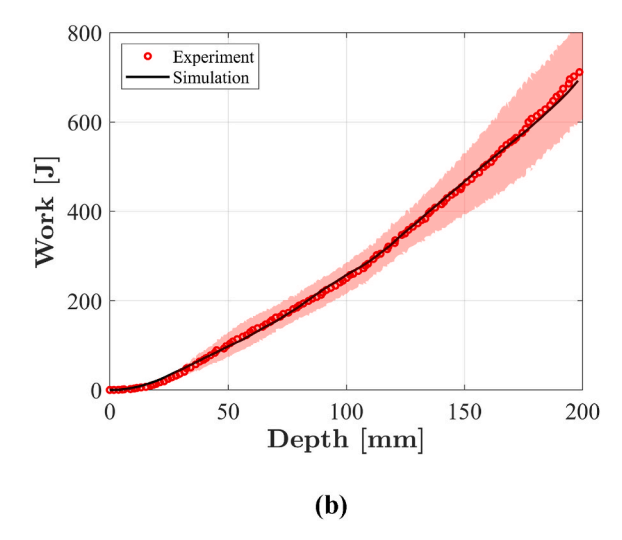


Fig. 16. Final verified simulation using the calibrated parameter set from GRSM method: (a) penetration resistance & (b) work done.

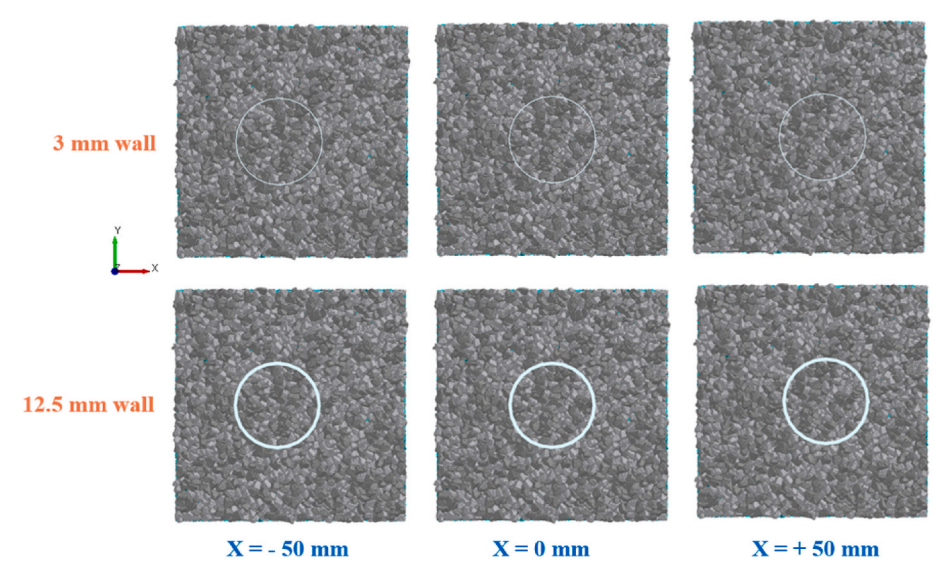


Fig. 17. Top view of the initial pile locations for the validation simulations.

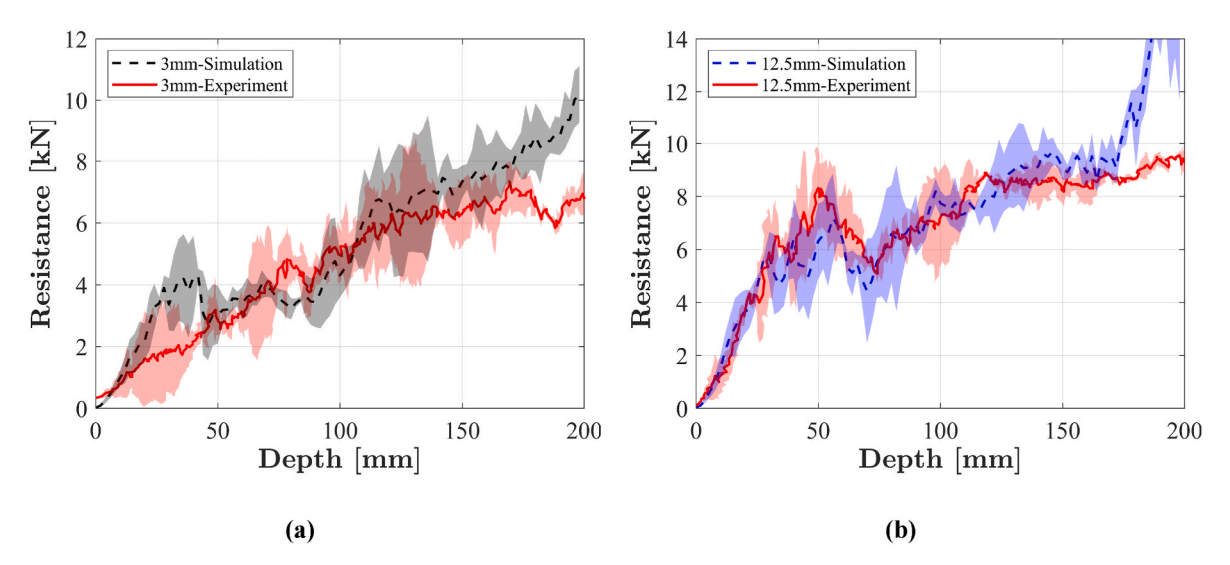


Fig. 18. Penetration resistance comparison between the experiments and the validation simulations using the mean values of simulations (n = 3) and individual tests of experiments for (a) 3 mm pile, and (b) 12.5 mm pile.

coefficients are limited to 0.4 and 0.5 by the full factorial DoE of the packing generation simulation.

- The model parameters of armour rocks are calibrated separately from those of filter rocks, and the global response search method (GRSM) is the most suitable optimisation method here for model calibration
- The simulation prediction of the calibrated and verified DEM model came into good agreement with the experimental measurements within the two rock layers (180 mm thickness). Furthermore, the standard deviations (variability) obtained from validation simulations are similar to those measured from the experiments in terms of magnitude, which further proves the predictability of the developed DEM model.

The results obtained here can be further used to complement labour and cost-intensive lab experiments and will also facilitate the efficient and accurate DEM modelling of multi-materials systems. Although the conclusions are valid only within the scope investigated in the current work, the proposed modelling framework is expected to have wider applicability in DEM model calibration, verification and validation.

Multiple assumptions are used in this study to achieve a computationally feasible modelling framework and these assumptions might not be valid in other systems, e.g., the cross-material interactions are less dominant due to the distinct layering of the materials. Future research can focus on modelling the systems where the cross-material interactions are of primary interest as well as upscaling the small-scale model to predict the pile penetration behaviours in the real field scale.

CRediT authorship contribution statement

Hao Shi: Writing – review & editing, Writing – original draft, Visualization, Software, Methodology, Investigation, Formal analysis, Data curation, Conceptualization. Cihan Cengiz: Writing – review & editing, Writing – original draft, Validation, Investigation, Data curation. Giulia Macaro: Writing – review & editing, Investigation, Data curation. Mario Martinelli: Writing – review & editing, Supervision, Data curation. Jovana Jovanova: Writing – review & editing, Writing – original draft, Supervision, Methodology, Investigation, Funding acquisition, Conceptualization. Dingena Schott: Writing – review & editing, Writing – original draft, Supervision, Software, Resources, Project administration,

Methodology, Funding acquisition, Conceptualization.

Declaration of competing interest

The authors declare that they have no known competing financial interests or personal relationships that could have appeared to influence the work reported in this paper.

Acknowledgements

This research was carried out under the OPIS project (HER+22-01-

03317702) supported by the Dutch Ministry of Economic Affairs and Climate Policy, Dutch Enterprise Agency (RVO) and TKI Offshore Energy. The authors would like to acknowledge the discussions and support from the GROW consortium partners: CAPE Holland B.V., DEME Offshore NL B.V., Equinor Holding Netherlands B.V., Heerema Engineering Solutions B.V., Heerema Marine Contractors Nederland SE, Jan de Nul N.V., Seaway 7 Offshore Contractors B.V., TenneT TSO B.V. and Vattenfall N.V.

Appendix A

Table A1
Final calibrated and verified sand material parameters on particle-particle (p-p) and particle-geometry (p-g) interactions.

| Symbol | Parameter Name [unit] | Value (scaled) |
|--------------------|--|--|
| ρ_p | Particle density [kg/m³] | 1664.3 |
| $\dot{\Phi}$ | Volume fraction | 0.63 |
| d_{10} | Particle diameter at 10% passing [mm] | 0.191 (1.91) |
| d_{50} | Particle diameter at 50% passing [mm] | 0.278 (2.78) |
| d_{90} | Particle diameter at 90% passing [mm] | 0.401 (4.01) |
| G_p | Particle shear modulus [GPa] | 0.05 (Combarros Garcia et al., 2016) |
| ν_{p} | Particle Poisson's ratio [-] | 0.25 (Combarros Garcia et al., 2016) |
| $\mu_{s,p-p}$ | Particle-particle sliding friction coefficient [-] | 0.64 (Combarros Garcia et al., 2016) |
| $\mu_{r,p-p}$ | Particle-particle rolling friction coefficient [-] | 0.1 (Combarros Garcia et al., 2016; Pereira, 1997) |
| e_{p-p} | Particle-particle restitution coefficient [-] | 0.75 (Combarros Garcia et al., 2016; Bărbunțoiu, 2021) |
| $\mu_{s,p-g}$ | Particle-geometry sliding friction coefficient [-] | 0.5 (Ucgul et al., 2015) |
| $\mu_{r,p-g}$ | Particle-geometry rolling friction coefficient [-] | 0.05 (Ucgul et al., 2015) |
| e_{p-g} | Particle-geometry restitution coefficient [-] | 0.6 (Ucgul et al., 2015; Das, 2019) |

Table A2
Final calibrated and verified armour material parameters on particle-particle (p-p) and particle-geometry (p-g) interactions.

| Symbol | Parameter Name [unit] | Value | |
|---------------|--|-------------------------------------|--|
| ρ_p | Particle density [kg/m ³] | 1680 | |
| Φ | Volume fraction | 0.60 | |
| d_{10} | Particle diameter at 10% passing [mm] | 17.06 | |
| d_{50} | Particle diameter at 50% passing [mm] | 25.81 | |
| d_{90} | Particle diameter at 90% passing [mm] | 31.56 | |
| G_p | Particle shear modulus [GPa] | 0.1 (Gupta and Seshagiri Rao, 2000) | |
| $\nu_{\rm p}$ | Particle Poisson's ratio [-] | 0.3 (Bărbunțoiu, 2021) | |
| $\mu_{s,p-p}$ | Particle-particle sliding friction coefficient [-] | 0.58 | |
| $\mu_{r,p-p}$ | Particle-particle rolling friction coefficient [-] | 0.5 | |
| e_{p-p} | Particle-particle restitution coefficient [-] | 0.5 | |
| $\mu_{s,p-g}$ | Particle-geometry sliding friction coefficient [-] | 0.95 | |
| $\mu_{r,p-g}$ | Particle-geometry rolling friction coefficient [-] | 0.5 | |
| e_{p-g} | Particle-geometry restitution coefficient [-] | 0.5 | |

Table A3
Final calibrated and verified filter material parameters on particle-particle (p-p) and particle-geometry (p-g) interactions.

| Symbol | Parameter Name [unit] | Value | |
|---------------|--|-------------------------------------|--|
| ρ_p | Particle density [kg/m³] | 1680 | |
| $\dot{\Phi}$ | Volume fraction | 0.54 | |
| d_{10} | Particle diameter at 10% passing [mm] | 5.31 | |
| d_{50} | Particle diameter at 50% passing [mm] | 6.56 | |
| d_{90} | Particle diameter at 90% passing [mm] | 9.31 | |
| G_p | Particle shear modulus [GPa] | 0.1 (Gupta and Seshagiri Rao, 2000) | |
| ν_p | Particle Poisson's ratio [-] | 0.3 (Bărbunțoiu, 2021) | |
| $\mu_{s,p-p}$ | Particle-particle sliding friction coefficient [-] | 0.72 | |
| $\mu_{r,p-p}$ | Particle-particle rolling friction coefficient [-] | 0.5 | |
| e_{p-p} | Particle-particle restitution coefficient [-] | 0.5 | |

(continued on next page)

Table A3 (continued)

| Symbol | Parameter Name [unit] | Value | |
|---------------------------------------|---|--------------------|--|
| $\mu_{s,p-g}$ $\mu_{r,p-g}$ e_{p-g} | Particle-geometry sliding friction coefficient [-] Particle-geometry rolling friction coefficient [-] Particle-geometry restitution coefficient [-] | 0.88 0.5 0.5 | |

References

- Ai, J., Chen, J.-F., Rotter, J.M., Ooi, J.Y., 2011. Assessment of rolling resistance models in discrete element simulations. Powder Technol. 206, 269–282. https://doi.org/ 10.1016/j.powtec.2010.09.030.
- Antony, J., 2023. Design of Experiments for Engineers and Scientists. Elsevier. Bărbunţoiu, T., 2021. Assessing the Drivability of a Monopile through the Rock Armour Layer: an Analysis Using Discrete Element Method and Small-Scale Testing, MSc. Thesis. TII Delft.
- Barbuntoiu, T., Thijssen, R., 2024. Monopile penetration through scour protection full scale testing and discrete element analysis. In: OnePetro. https://doi.org/10.4043/35312.MS
- Cao, Y., Bai, Y., Wang, J., Liao, S., Xu, D., 2015. Prediction of scour depth around offshore pipelines in the South China Sea. J. Marine. Sci. Appl. 14, 83–92. https:// doi.org/10.1007/s11804-015-1290-1.
- Cerfontaine, B., Brown, M.J., Ciantia, M., Huisman, M., Ottolini, M., 2021a. Discrete element modelling of silent piling group installation for offshore wind turbine foundations. In: Proceedings of the Second International Conference on Press-In Engineering 2021. CRC Press, Kochi, Japan.
- Cerfontaine, B., Ciantia, M., Brown, M.J., Sharif, Y.U., 2021b. DEM study of particle scale and penetration rate on the installation mechanisms of screw piles in sand. Comput. Geotech. 139, 104380. https://doi.org/10.1016/j.compgeo.2021.104380.
 Cerfontaine, B., Ciantia, M.O., Brown, M.J., White, D.J., Sharif, Y.U., 2023. DEM study of
- Cerfontaine, B., Ciantia, M.O., Brown, M.J., White, D.J., Sharif, Y.U., 2023. DEM study of particle scale effect on plain and rotary jacked pile behaviour in granular materials. Comput. Geotech. 161, 105559. https://doi.org/10.1016/j.compge0.2023.105559.
- Chakrabarty, A., Biswas, R., Basu, S., Nag, S., 2022. Characterisation of binary mixtures of pellets and sinter for DEM simulations. Adv. Powder Technol. 33, 103358. https://doi.org/10.1016/j.apt.2021.11.010.
- Chen Ong, M., Trygsland, E., Myrhaug, D., 2017. Numerical study of seabed boundary layer flow around monopile and gravity-based wind turbine foundations. J. Offshore Mech. Arctic Eng. 139. https://doi.org/10.1115/1.4036208.
- Cheng, X., Wang, T., Zhang, J., Liu, Z., Cheng, W., 2021. Finite element analysis of cyclic lateral responses for large diameter monopiles in clays under different loading patterns. Comput. Geotech. 134, 104104. https://doi.org/10.1016/j. compage 2021 104104
- Coetzee, C.J., 2017. Review: calibration of the discrete element method. Powder Technol. 310, 104–142. https://doi.org/10.1016/j.powtec.2017.01.015.
- Coetzee, C.J., 2019. Particle upscaling: calibration and validation of the discrete element method. Powder Technol. 344, 487–503. https://doi.org/10.1016/j. powtec.2018.12.022.
- Combarros Garcia, M., Feise, H.J., Strege, S., Kwade, A., 2016. Segregation in heaps and silos: comparison between experiment, simulation and continuum model. Powder Technol. 293, 26–36. https://doi.org/10.1016/j.powtec.2015.09.036.
- Dahlberg, R., 1983. Observations of scour around offshore structures. Can. Geotech. J. 20, 617–628. https://doi.org/10.1139/t83-071.
- Das, B.M., 2019. Advanced Soil Mechanics, fifth ed. CRC Press, London. https://doi.org/10.1201/9781351215183.
- Di Renzo, A., Di Maio, F.P., 2005. An improved integral non-linear model for the contact of particles in distinct element simulations. Chem. Eng. Sci. 60, 1303–1312. https://doi.org/10.1016/j.ces.2004.10.004.
- DNV, 2022. Rock Scour Protection for Monopiles. DNV-RP-0618.
- Do, H.Q., Aragón, A.M., Schott, D.L., 2018. A calibration framework for discrete element model parameters using genetic algorithms. Adv. Powder Technol. 29, 1393–1403. https://doi.org/10.1016/j.apt.2018.03.001.
- Durda, D.D., Movshovitz, N., Richardson, D.C., Asphaug, E., Morgan, A., Rawlings, A.R., Vest, C., 2011. Experimental determination of the coefficient of restitution for meterscale granite spheres. Icarus 211, 849–855. https://doi.org/10.1016/j. icarus 2010.09.003
- Emmerink, J., Hadi, A., Jovanova, J., Cleven, C., Schott, D.L., 2023. Parametric analysis of a double Shaft, batch-type paddle mixer using the discrete element method (DEM). Processes 11, 738. https://doi.org/10.3390/pr11030738.
- Esposito, R.G., Velloso, R.Q., Jr, E. do A.V., Danziger, B.R., 2018. Multi-scale sensitivity analysis of pile installation using DEM, Comp. Part. Mech 5, 375–386. https://doi. org/10.1007/s40571-017-0175-2.
- Feng, Y., Blumenfeld, R., Liu, C., 2019. Support of modified Archimedes' law theory in granular media. Soft Matter 15, 3008–3017. https://doi.org/10.1039/C8SM02480D.
- Fuchs, R., Weinhart, T., Meyer, J., Zhuang, H., Staedler, T., Jiang, X., Luding, S., 2014. Rolling, sliding and torsion of micron-sized silica particles: experimental, numerical and theoretical analysis. Granul. Matter 16, 281–297. https://doi.org/10.1007/ s10035-014-0481-9.
- Gerwick Jr., B.C., 2007. Construction of Marine and Offshore Structures. CRC press
- Gezgin, A.T., Soltanbeigi, B., Cinicioglu, O., 2022. Discrete-element modelling of pile penetration to reveal influence of soil characteristics. Proceedings of the Institution

- of Civil Engineers Geotechnical Engineering 175, 365–382. https://doi.org/
- Grima, A.P., Wypych, P.W., 2011. Development and validation of calibration methods for discrete element modelling. Granul. Matter 13, 127–132. https://doi.org/ 10.1007/s10035-010-0197-4.
- Gupta, A.S., Seshagiri Rao, K., 2000. Weathering effects on the strength and deformational behaviour of crystalline rocks under uniaxial compression state. Eng. Geol. 56, 257–274. https://doi.org/10.1016/S0013-7952(99)00090-3.
- Hadi, A., Shi, H., Pang, Y., Schott, D., 2024. Identification of dominant DEM parameters for multi-component segregation during heap formation, hopper discharge and chute flow. Powder Technol. 444, 119985. https://doi.org/10.1016/j. powtec.2024.119985.
- Hageman, E., 2022. Simulating Monopile Installation through Scour Protection Using the Discrete Element Method. TU Delft. MSc thesis.
- Horst, R., Pardalos, P.M., 2013. Handbook of Global Optimization. Springer Science & Business Media.
- Huang, X., Hanley, K.J., O'Sullivan, C., Kwok, C.Y., 2014. Exploring the influence of interparticle friction on critical state behaviour using DEM. Int. J. Numer. Anal. Methods GeoMech. 38, 1276–1297. https://doi.org/10.1002/nag.2259.
- Imre, B., Räbsamen, S., Springman, S.M., 2008. A coefficient of restitution of rock materials. Comput. Geosci. 34, 339–350. https://doi.org/10.1016/j. cage0.2007.04.004.
- Jaiman, R.K., Shakib, F., Oakley, O.H., Constantinides, Y., 2010. Fully Coupled Fluid-Structure Interaction for Offshore Applications. American Society of Mechanical Engineers Digital Collection, pp. 757–765. https://doi.org/10.1115/OMAE2009-79804.
- James, C.S., 2020. Scour and scour protection. In: James, C.S. (Ed.), Hydraulic Structures. Springer International Publishing, Cham, pp. 319–363. https://doi.org/ 10.1007/978-3-030-34086-5 9.
- Leimeister, M., Dose, B., 2018. Validation and Development of Improved Methods for the Calculation of Wave Loads on XXL Monopiles. American Society of Mechanical Engineers Digital Collection. https://doi.org/10.1115/OMAE2018-77232.
- Li, Q., Prendergast, L.J., Gavin, K.G., Askarinejad, A., Wang, X.Q., 2024. A method to quantify the beneficial effect of scour protection on lateral behaviour of monopiles for offshore wind turbines. Ocean Engineering 307, 118196. https://doi.org/ 10.1016/i.oceaneng.2024.118196.
- Liu, H., Kaynia, A.M., 2022. Monopile responses to monotonic and cyclic loading in undrained sand using 3D FE with SANISAND-MSu. Water Sci. Eng. 15, 69–77. https://doi.org/10.1016/j.wse.2021.12.001.
- Liu, S., Wang, J., 2016. Depth-independent cone penetration mechanism by a discrete element method (DEM)-based stress normalization approach. Can. Geotech. J. 53, 871–883. https://doi.org/10.1139/cgj-2015-0188.
- Locatelli, M., Schoen, F., 2013. Global Optimization: Theory, Algorithms, and Applications. SIAM.
- Lommen, S., 2016. Virtual Prototyping of Grabs: Co-simulations of Discrete Element and Rigid Body Models. TU Delft.
- Lommen, S., Mohajeri, M., Lodewijks, G., Schott, D., 2019. DEM particle upscaling for large-scale bulk handling equipment and material interaction. Powder Technol. 352, 273–282. https://doi.org/10.1016/j.powtec.2019.04.034.
- Ma, H., Chen, C., 2021. Scour protection assessment of monopile foundation design for offshore wind turbines. Ocean Engineering 231, 109083. https://doi.org/10.1016/j. oceaneng.2021.109083.
- Mandviwalla, X., Christensen, E.D., 2021. Entrainment of sediment particles in protection layers. J. Hydraul. Eng. 147, 04021040. https://doi.org/10.1061/(ASCE) HV 1943-7900 0001898
- Marigo, M., Stitt, E.H., 2015. Discrete element method (DEM) for Industrial applications: Comments on calibration and validation for the modelling of Cylindrical pellets. KONA Powder and Particle Journal 32, 236–252. https://doi.org/10.14356/kona.2015016.
- Mayall, R.O., McAdam, R.A., Whitehouse, R.J.S., Burd, H.J., Byrne, B.W., Heald, S.G., Sheil, B.B., Slater, P.L., 2020. Flume Tank testing of offshore wind turbine dynamics with foundation scour and scour protection. J. Waterw. Port, Coast. Ocean Eng. 146, 04020033. https://doi.org/10.1061/(ASCE)WW.1943-5460.0000587.
- Mindlin, R.D., 1949. Compliance of elastic Bodies in contact. J. Appl. Mech. 16, 259–268. https://doi.org/10.1115/1.4009973.
- Mindlin, R.D., 1964. Micro-structure in linear elasticity. Arch. Ration. Mech. Anal. V16. https://doi.org/10.1007/BF00248490.
- Miyai, S., Kobayakawa, M., Tsuji, T., Tanaka, T., 2019. Influence of particle size on vertical plate penetration into dense cohesionless granular materials (large-scale DEM simulation using real particle size). Granul. Matter 21, 105. https://doi.org/ 10.1007/s10035-019-0961-z.
- Mohajeri, M.J., Do, H.Q., Schott, D.L., 2020. DEM calibration of cohesive material in the ring shear test by applying a genetic algorithm framework. Adv. Powder Technol. 31, 1838–1850. https://doi.org/10.1016/j.apt.2020.02.019.

- Netherlands Enterprise Agency, 2022. Scour and Scour Mitigation for Ten noorden van de Waddeneilanden Wind Farm Zone.
- Nietiedt, J.A., Randolph, M.F., Gaudin, C., Doherty, J.P., 2023a. Centrifuge model tests investigating Initiation and Propagation of pile tip damage during driving. J. Geotech. Geoenviron. Eng. 149, 04023024. https://doi.org/10.1061/JGGEFK. GTFNG-10616
- Nietiedt, J.A., Randolph, M.F., Gaudin, C., Doherty, J.P., 2023b. Preliminary assessment of potential pile tip damage and extrusion buckling. Ocean Engineering 275, 114071. https://doi.org/10.1016/j.oceaneng.2023.114071.
- Ooi, J.Y., 2013. Establishing predictive capabilities of DEM verification and validation for complex granular processes. AIP Conf. Proc. 1542, 20–24. https://doi.org/ 10.1063/1.4811861
- OuYang, H., Dai, G., Gao, L., Zhu, W., Du, S., Gong, W., 2022. Local scour characteristics of monopile foundation and scour protection of cement-improved soil in marine environment - laboratory and site investigation. Ocean Engineering 255, 111443. https://doi.org/10.1016/j.oceaneng.2022.111443.
- Pardalos, P.M., Romeijn, H.E., 2013. Handbook of Global Optimization, ume 2. Springer Science & Business Media.
- Pereira, J.P., 1997. Rolling friction and shear behaviour of rock discontinuities filled with sand. Int. J. Rock Mech. Min. Sci. 34, 244.e1–244.e17. https://doi.org/ 10.1016/S1365-1609(97)00037-3.
- Roessler, T., Katterfeld, A., 2018. Scaling of the angle of repose test and its influence on the calibration of DEM parameters using upscaled particles. Powder Technol. 330, 58–66. https://doi.org/10.1016/j.powtec.2018.01.044.
- Sandeep, C.S., Senetakis, K., Cheung, D., Choi, C.E., Wang, Y., Coop, M.R., Ng, C.W.W., 2021. Experimental study on the coefficient of restitution of grain against block interfaces for natural and engineered materials. Can. Geotech. J. 58, 35–48. https:// doi.org/10.1139/cgj-2018-0712.
- Sarımurat, S., 2023. Investigation of the effects of cyclic lateral load characteristics on monopiles in saturated sandy soils using hypoplastic material model. Wind Energy 26, 1165–1187. https://doi.org/10.1002/we.2862.
- Shapiro, J., 2001. Genetic algorithms in Machine Learning. In: Paliouras, G., Karkaletsis, V., Spyropoulos, C.D. (Eds.), Machine Learning and its Applications: Advanced Lectures. Springer, Berlin, Heidelberg, pp. 146–168. https://doi.org/ 10.1007/3-540-44673-7_7.
- Shi, H., Roy, S., Weinhart, T., Magnanimo, V., Luding, S., 2020. Steady state rheology of homogeneous and inhomogeneous cohesive granular materials. Granul. Matter 22,
- Singh, N.B., Devi, T.T., Kumar, B., 2022. The local scour around bridge piers—a review of remedial techniques. ISH Journal of Hydraulic Engineering 28, 527–540. https:// doi.org/10.1080/09715010.2020.1752830.
- Tran, T.T., Kim, D.-H., 2018. A CFD study of coupled aerodynamic-hydrodynamic loads on a semisubmersible floating offshore wind turbine. Wind Energy 21, 70–85. https://doi.org/10.1002/we.2145.

- Tripathi, A., Kumar, V., Agarwal, A., Tripathi, A., Basu, S., Chakrabarty, A., Nag, S., 2021. Quantitative DEM simulation of pellet and sinter particles using rolling friction estimated from image analysis. Powder Technol. 380, 288–302. https://doi.org/10.1016/j.powtec.2020.11.024.
- Ucgul, M., Fielke, J.M., Saunders, C., 2015. Defining the effect of sweep tillage tool cutting edge geometry on tillage forces using 3D discrete element modelling. Information Processing in Agriculture 2, 130–141. https://doi.org/10.1016/j. ippa. 2015.07.001
- Varelis, G.E., Ai, J., Kane, P., Ragheb, H., Dib, E., 2021. Scour Effects on the Structural Integrity of Offshore Wind Turbine Monopiles. American Society of Mechanical Engineers Digital Collection. https://doi.org/10.1115/IOWTC2021-3554.
- Wang, H., Wang, L., Hong, Y., Masín, D., Li, W., He, B., Pan, H., 2021. Centrifuge testing on monotonic and cyclic lateral behavior of large-diameter slender piles in sand. Ocean Engineering 226, 108299. https://doi.org/10.1016/j.oceaneng.2020.108299.
- Wang, G., Xu, S., Zhang, Q., Zhang, J., 2023. An experimental study of the local scour protection methods around the monopile foundation of offshore wind turbines. Ocean Engineering 273, 113957. https://doi.org/10.1016/j.oceaneng.2023.113957.
- Wensrich, C.M., Katterfeld, A., 2012. Rolling friction as a technique for modelling particle shape in DEM. Powder Technol. 217, 409–417. https://doi.org/10.1016/j. powtec 2011.10.057
- Whitehouse, R.J.S., Harris, J.M., Sutherland, J., Rees, J., 2011. The nature of scour development and scour protection at offshore windfarm foundations. Mar. Pollut. Bull. 62, 73–88. https://doi.org/10.1016/j.marpolbul.2010.09.007.
- Winkler, K., Weil, M., Jurado, C.S., Stuyts, B., Weijtjens, W., Devriendt, C., 2023. Quantifying the effect of rock armour scour protection on eigenfrequencies of a monopile supported OHVS. J. Phys.: Conf. Ser. 2626, 012039. https://doi.org/ 10.1088/1742-6596/2626/1/012039.
- Zhai, Y., Christensen, E.D., 2022. Computational fluid dynamics investigation of flow in scour protection around a Mono-pile with the volume-averaged k-ω model.

 J. Offshore Mech. Arctic Eng. 144. https://doi.org/10.1115/1.4054393.
- Zhang, Z., Wang, Y.-H., 2015. Three-dimensional DEM simulations of monotonic jacking in sand. Granul. Matter 17, 359–376. https://doi.org/10.1007/s10035-015-0562-4.
- Zhang, Y., Zhao, M., Kwok, K.C.S., Liu, M.M., 2015. Computational fluid dynamics-discrete element method analysis of the onset of scour around subsea pipelines. Appl. Math. Model. 39, 7611–7619. https://doi.org/10.1016/j. apm.2015.03.058.
- Zhang, F., Chen, X., Yan, J., Gao, X., 2023a. Countermeasures for local scour around offshore wind turbine monopile foundations: a review. Appl. Ocean Res. 141, 103764. https://doi.org/10.1016/j.apor.2023.103764.
- Zhang, S., Li, B., Ma, H., 2023b. Numerical investigation of scour around the monopile using CFD-DEM coupling method. Coastal Engineering 183, 104334. https://doi. org/10.1016/j.coastaleng.2023.104334.
- Zhu, H.P., Zhou, Z.Y., Yang, R.Y., Yu, A.B., 2007. Discrete particle simulation of particulate systems: theoretical developments. Chem. Eng. Sci. 62. https://doi.org/ 10.1016/j.ces.2006.12.089.